communications
earth & environment

ARTICLE

https://doi.org/10.1038/s43247-023-00956-6 OPEN

Refertilized continental root controls the formation of the Mianning–Dechang carbonatite-associated rare-earth-element ore system

Zeng-Qian Hou[1]✉, Bo Xu[2]✉, Haijiang Zhang[3]✉, Yuan-Chuan Zheng[2], Rui Wang[2], Yan Liu[1], Zhuang Miao[2], Lei Gao[3], Zhidan Zhao[2], William L. Griffin[4] & Suzanne Y. O'Reilly[4]

Rare earth element ore deposits associated with carbonatite derived from Earth's mantle supply half of the world's rare earth element. However, the formation of carbonatite and initial enrichment and transport of rare earth element in the mantle, is unclear. Here, we image the lithospheric architecture of a Cenozoic rare earth element ore belt in southwestern China by integrating seismic tomography with geochemical data. The subduction of the Indian continent caused vertical upwelling and lateral flow of the asthenosphere, which triggered the melting of the overlying subcontinental lithospheric mantle to generate carbonatites. Such a mantle source that previously metasomatized by fluids from recycled marine sediments is a precursor process critical for forming a giant rare earth element system. For the studied ore belt, three key factors are prerequisites to generating ore-forming carbonatites: thick lithosphere with a continental root; prior fertilization of the subcontinental lithospheric mantle; and trans-lithospheric weakness for magma ascent.

[1] SinoProbeLab, Institute of Geology, CAGS, 100037 Beijing, China. [2] State Key Laboratory of Geological Processes and Mineral Resources, China University of Geosciences, 100083 Beijing, China. [3] School of Earth and Space Sciences, University of Science and Technology of China, 230026 Hefei, China. [4] ARC Centre of Excellence for Core to Crust Fluid Systems (CCFS) and GEMOC, Macquarie University, Sydney, NSW 2109, Australia. ✉email: houzengqian@126.com; bo.xu@cugb.edu.cn; zhang11@ustc.edu.cn

Rare-earth elements (REEs) are essential for many high-technology applications, new energy industries, and defense systems. Thus, understanding the processes by which they are concentrated and trapped in the crust is currently a focus of investigations. REE deposits come in a wide variety[1,2], and carbonatite-associated REE deposits (CARD) are among the most significant types, which supply half of the world's REE + Y(yttrium)[1,3,4] and thus are prime targets for focused exploration[5,6].

About 527 carbonatite occurrences are exposed on all of Earth's continents[7–9], and 75% of them are emplaced within 600 km of craton edges[10]. These carbonatites may have been directly erupted from their mantle sources or frequently emplaced after protracted modification within the lithosphere[9]. They mainly occur as circular to ovoid complexes in continental rifts (e.g., East Africa) and orogenic belts (e.g., southwestern China) but are also associated with large igneous provinces (e.g., Deccan) and/or alkaline provinces (e.g., Greenland and the Kola Peninsula)[10,11]. A commonly held view suggests that carbonatites originate from an enriched or metasomatized mantle source[10], but the relative roles of the lithosphere and asthenosphere in carbonatite formation have been controversial[8,12–16]. A crucial assessment of these controversies requires a close examination of the underlying mantle structure and its plausible evolution.

Explorations show that only a few carbonatites host giant and large-sized CARDs[2,4–6,17]. These CARDs mainly form in continental rift settings (e.g., Bayun Obo in north China)[18] and syn- to post-collisional settings (e.g., Maoniuping in southwest China)[17,19,20]. The associated magmas are regarded to have been derived from the subcontinental lithospheric mantle (SCLM)[21,22], enriched by plume activity or previous subduction[2,8,22–24]. Recent studies indicate that the total resources of such CARDs are controlled by the volume of the parent magmas and the availability of enriched mantle sources[2] and that primary REE-poor orogenic carbonatites can be enriched by early processes of metasomatism[22]. However, how the mantle architecture influences lithosphere focusing and how REEs are fertilized in the metasomatized SCLM and later transported out of the mantle for the formation of CARDs remain unclear. We demonstrate that the key to understanding these issues is deciphering the lithospheric architecture and deep processes beneath REE-rich young orogens at cratonic edges.

The eastern Tibetan orogen, formed by the Cenozoic Indo-Asian collision[19], hosts a REE ore system—the Cenozoic Mianning–Dechang (MD) REE belt[20] (Fig. 1a). This orogen is an ideal place to investigate the factors controlling CARD formation because of its young mineralization age (27–12 Ma) without later reworking[25], a clearly defined post-collisional setting for their occurrence[22], and the current lithospheric structure without noticeable modification after the CARD formation. The MD REE belt was developed along the western margin of the Yangtze craton, where the exposed remnants of 1000–740 Ma arc volcanic rocks and granitoids recorded the Neoproterozoic accretion related to subduction[26], and Cenozoic reworking by the Indo-Asian collision produced numerous Cenozoic strike-slip fault systems (e.g., Red-River fault [RRF], Xiaojiang fault [XJF], and Xianshuihe fault) in the orogen[19] (Fig. 1a). This collision also caused extensive Eocene potassic–ultrapotassic magmatism along the RRF (Fig. 1a)[21,27] and formed a NS-trending 200-km-long REE-rich complex belt (i.e., MD REE belt) along the XJF at the cratonic edge[20,21]. This belt is composed of numerous carbonatite–syenite complexes (30–12 Ma), which host several CARDs, such as the giant Maoniuping (22 Ma), large-sized Dalucao (12 Ma), and medium Lizhuang (27 Ma)[20,25], constituting a Cenozoic giant REE ore system along the cratonic margin (Fig. 1a).

Here, we reveal the lithospheric architecture and deep processes of the MD REE belt by integrating a P-wave tomography model with geochemical data over an area covering the Tibetan orogen to the Yangtze craton. Our results provide a framework to probe the genesis of CARDs and their controlling factors, and the resulting genetic model provides a useful reference for the exploration of such CARDs.

Results and discussion

Lithospheric architecture imaged through seismic tomography. Seismic images with different resolutions have revealed the crust- and uppermost-mantle velocity structures in Tibet[28,29]. In this study, the teleseismic double-difference seismic tomography method was used to image the lithospheric architecture that controls the CARD formation using seismic arrival times from earthquakes within and surrounding the China continent recorded by local, regional, and teleseismic stations (see "Methods" and Supplementary Figs. 1–8).

Our P-wave images clearly show both the Indian and Yangtze blocks as high-Vp anomalies at depths of 160 and 80 km, respectively, with boundaries around longitudes 98–99°E (Fig. 1b), consistent with previous result[29]. The two high-velocity bodies are contiguous around latitudes 28–30°N (Fig. 1b), indicating that the two blocks collided at this location, thus controlling lithospheric deformation in the orogen. We interpret the high-Vp boundary of the Indian block as the northeastern front of the Indian lithospheric mantle (Fig. 1b)[30]. There are two large regions of low-velocity anomalies to the north and south of this convergent zone, again consistent with previous results[31]. These two low-velocity regions may be connected by a low-velocity channel between the Indian and Yangtze blocks at depths of 80–110 km around longitude 99°E, as evidenced by a high-resolution lithosphere Vs model for continental China (Supplementary Fig. 8b)[32]. Both regions are also spatially correlated with Cenozoic mantle-derived magmatic provinces at the surface (Fig. 1a), high-temperature mantle domains (1200 °C)[33], and mantle He in modern hydrothermal reservoirs (Fig. 1b)[34].

The three roughly E-W or NE-SW profiles show that the subducted Indian lithosphere (high Vp) reached the mantle transition zone, or even deeper, at a high angle with slight flattening in the north (Fig. 2a) and steepening in the south (Fig. 2b). Along the RRF and the adjacent region at 97–101°E, a remarkable feature of the P-wave image is the occurrence of a large mushroom-shaped low-velocity body. Its stem is rooted at depths >400 km, and the head extends laterally beneath the rigid Yangtze mantle lithosphere (Fig. 2b, c), locally stretching upward to the crust–mantle boundary (Fig. 2a). The overlying lithosphere shows obvious velocity heterogeneities. In the south, a large high-velocity body indicates that the orogenic lithosphere is relatively intact and thick (Figs. 1b and 2c). To the north, the cratonic lithosphere becomes thin (~100 km) and disjointed, as shown by two distinct and separated, relatively weak high-velocity domains beneath the Yangtze craton (Fig. 2b). We interpret this large low-velocity body as a large-scale asthenospheric upwelling focused along the block boundaries, thermally eroding and reworking the overlying lithosphere at the cratonic margin.

Along the western margin of the Yangtze craton at approximately 102°E, there are widely distributed shallow low-velocity anomalies (Fig. 2a, b), coinciding with the MD REE belt around the XJF system[35]. They occur along a N-S-striking Cenozoic strike-slip fault system superposed on a Permian rift[21] and become weak southward at 26°N, where the MD REE belt disappears (Fig. 2a). These shallow low-velocity anomalies extend down to an ~100-km depth and connect with a large underlying low-velocity body through a tilted low-velocity band, which

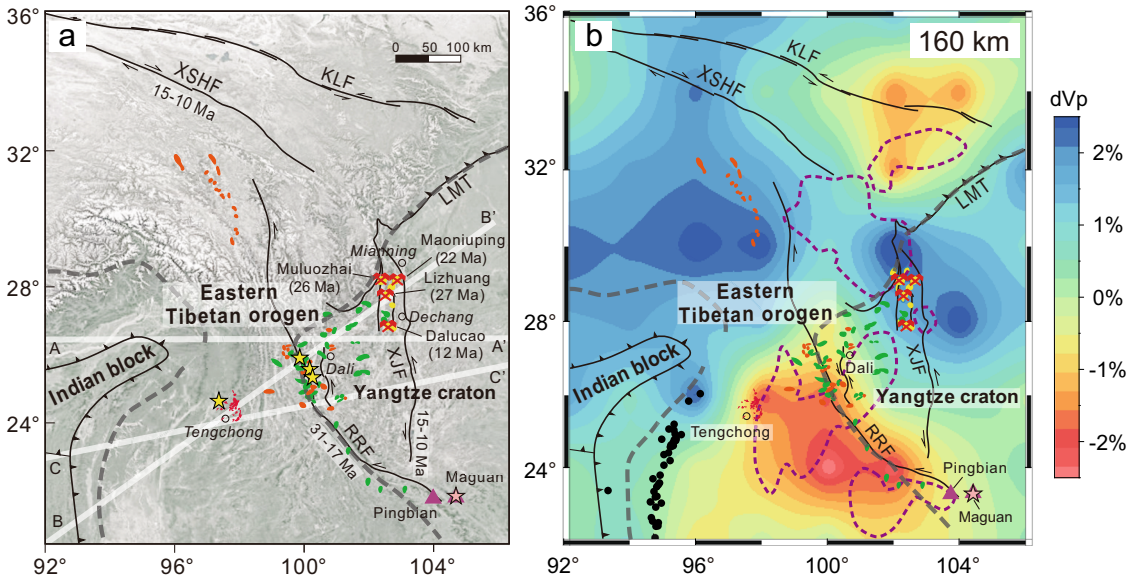

Fig. 1 Topographic-geological map and P-wave velocity image of the Yangtze craton and the Tibetan orogen. a shows a tectonic framework of the Tibetan orogen and craton (modified from ref. [19] and ref. [39]), in which the Cenozoic CARDs (red hammers), including the giant Maoniuping (22 Ma), the large Dalucao (12 Ma), the medium Lizhuang (27 Ma), and the small Muluozhai (26 Ma)[20,25], are shown. Black dotted lines are the boundaries of the Indian block and Yangtze craton. Black lines are the Cenozoic strike-slip faults (KLF: Kara–Kunlun fault; XSHF: Xianshuihe fault; RRF: Red-River fault; XJF: Xiaojiang faults) and thrust fault (LMT: Longenshan fault) with ages labeled. The Cenozoic magmatic rocks are shown as follows: Tengchong basalts (red, 2.7–0.2 Ma), Eocene–Pliocene ultrapotassic (green, 37–30 Ma) and potassic rocks along the RRF (orange, 43–32 Ma), Oligocene-Miocene carbonate-syenite complexes in the MD REE belt (yellow, 30–10 Ma), and Miocene ocean-island basalt (OIB) (mauve triangle, 13–1.7 Ma). Pink star: mantle xenolith locality; yellow stars: crustal xenolith localities. The positions of three seismic profiles across the MD REE belt are shown. **b** shows a P-wave velocity slice at depth of 160 km in the study area. The domains of mantle-derived He gas in modern springs (purple dotted line) are also shown.

separates the Yangtze lithosphere into two segments with distinct thicknesses (Fig. 2a, b). This structure is also imaged by receiver function results[36], which can be interpreted as representing the eastward lateral flow of the asthenosphere and its subsequent upwelling along the trans-lithospheric faults. The lateral flow of the asthenosphere is also supported by the dominant E-W fast polarizations of teleseismic SKS waves from shear wave splitting analysis in this area[37,38].

New and previously-published geochemical data further constrain the lithospheric architecture imaged by seismic tomography (Supplementary Data 1–3). The explosive ultrapotassic magmas with eruption ages peaking at 35 ± 2 Ma are extensively developed along the RRF (Fig. 1a), and their geochemical signatures suggest a derivation from partial melting of metasomatized SCLM (Supplementary Figs. 9 and 10)[27,39] at an ~80-km depth (Fig. 3a). This process is consistent with our seismic images (Fig. 2a, b) and high estimated temperatures of the upper mantle (Fig. 3a), confirming that the cratonic SCLM was disrupted, thinned, and partially melted by the asthenospheric upwelling along the RRF. Coeval potassic granitoids in Dali, showing geochemical affinity with adakites, are considered to have originated from the collision-thickened (45- to 50-km) mafic lower crust in the orogen[40] (Fig. 3a). Our seismic images also reveal that the orogenic lower crust was heated by high heat flows from the upwelling asthenosphere, resulting in the upward percolation of small-volume mantle melts (Fig. 2a). Minor Quaternary basalts (13–0.3 Ma) locally developed after the main magmatic event (~35 Ma) along the RRF (Fig. 1a). These basalts contain mantle xenoliths and show geochemical affinity with oceanic island basalts (OIBs)[19,39], suggesting decompression melting of the asthenosphere during upwelling since the mid-Miocene. All these observations point to a consistent interpretation—that the steep subduction of the Indian continental lithosphere led to continuous asthenospheric upwelling, thermal erosion, partial melting, and interaction with the overlying cratonic lithosphere since ~35 Ma.

The partial melting of the SCLM focused at 35 Ma is not limited to the RRF but also extends eastward across the RRF, at times ranging from 35 to 12 Ma (Fig. 2a–c). The eastward lateral flow is supported by the eastward prolongation of the ultrapotassic magmatism (35–30 Ma) and its association with the MD carbonatites (30–12 Ma; Fig. 1a). The westward flow is recorded by Quaternary calc-alkaline lavas (14–0.2 Ma) in Tengchong. Their arc-like signature and the enriched Sr–Nd isotope compositions suggest a derivation from the mantle wedge, previously metasomatized by Neo-Tethyan oceanic subduction (Supplementary Figs. 9–11) but heated by the westward asthenospheric upwelling since 14 Ma (Fig. 3a).

Three lines of evidence further confirm the asthenospheric upwelling in the Cenozoic. First, electron backscattered diffraction studies of mantle xenoliths hosted by OIB-like basalts at Maguan (Fig. 1a) show strong deformation fabrics, recording a vertical flow of mantle material[41], and their equilibration temperatures are estimated at >1200 °C, much higher than that predicted by a cratonic geotherm[42]. Secondly, lower crustal xenoliths from Tengchong and Dali (Fig. 1a) underwent high-temperature granulite- and amphibolite-facies metamorphism at very high equilibration temperatures (1050 °C–900 °C)[43]. Third, P-T-t paths for the metamorphic belts along the RRF reflect a complex process evolving from heating and ductile flow at 40–35 Ma to brittle shear at 30–23 Ma[44]. Therefore, we conclude that the subduction of the Indian lithosphere during collision induced the upwelling of the Asian asthenosphere, thus changing the cratonic–orogenic lithospheric thermal regime, triggering its partial melting and controlling crustal deformation in the orogen.

Carbonatite formed by melting of the metasomatized SCLM. Previous modeling, overwhelmingly based on geochemical and Sr,

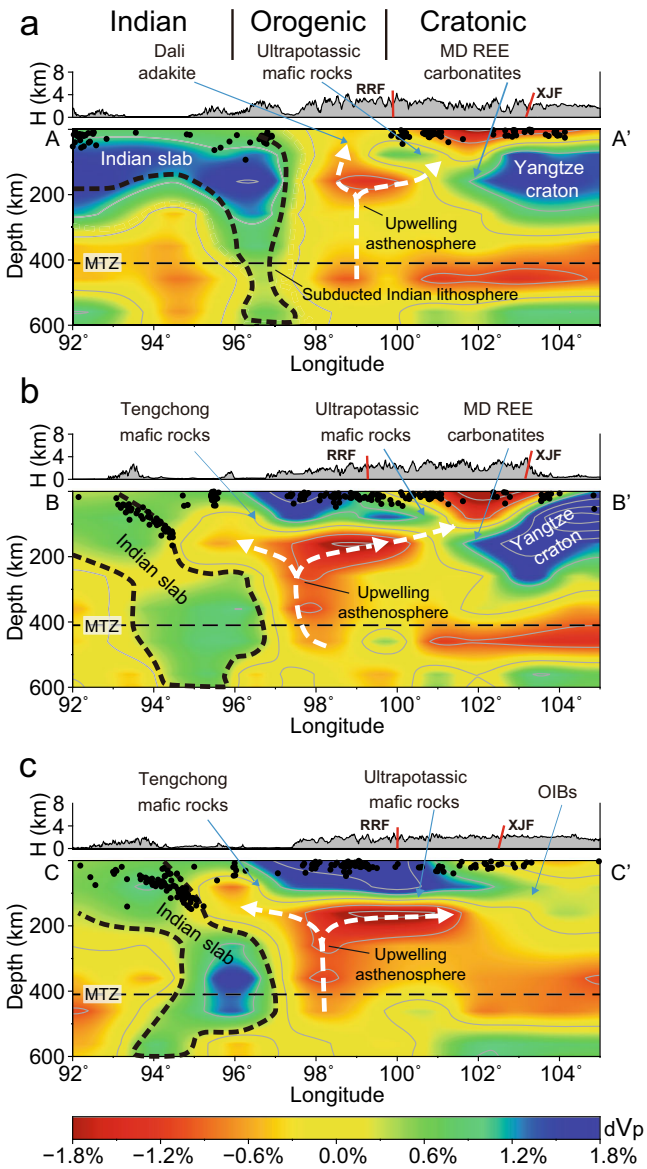

Fig. 2 Images of the Vp structures along three profiles. a–c represent profiles A-A′, B-B′, and C-C′ in Fig. 1a respectively. Geological interpretation is based on seismic velocity and geological observations. Sources of Cenozoic magma and faults were shown. White dotted lines with arrows refer to upwelling and lateral flow of upwelling asthenosphere. MTZ mantle transition zone, RRF Red-River fault, XJF Xiaojiang fault.

Nd, Pb, O, and C isotope data of carbonatites worldwide, suggested distinct mantle sources for their genesis, such as the asthenosphere related to plume activity[8,12], heterogeneous lithospheric mantle[15], and mixing source between the lithosphere and asthenosphere[14,16]. Three lines of evidence suggest that the MD carbonatites originated from the cratonic SCLM with variable degrees of metasomatism[22], except for the carbonatite at Dalucao showing crustal contribution[21,23,24]. First, these carbonatites have more radiogenic Sr–Nd isotope compositions with initial $(^{87}Sr/^{86}Sr)_i$ of 0.7056–0.7080 and $\varepsilon_{Nd}(t)$ of −6.0 to −1.6[19,21,22], overlapping with those of the Eocene ultrapotassic rocks that originated from the metasomatized cratonic SCLM[22,45] (Fig. 3b). Second, the associated syenites yielded similar Sr–Nd isotope compositions, with initial $^{87}Sr/^{86}Sr = 0.7043–0.7049$ and $\varepsilon_{Nd}(t)$ from −2.4 to −6.5[39], suggesting a genetic link. Thirdly, the magmatic zircons from these syenites yielded $\delta^{18}O$ of +3.8 to +5.4‰ and εHf of −3.7 to +1.2, also indicating a SCLM source with minor marine sediments (Supplementary Fig. 11).

Figure 2a, b clearly shows that the MD carbonatite belt spatially coincides with an underlying shallow low-velocity mantle zone, which could be attributed to the presence of low-viscosity carbonate melts or volatiles (CO_2, H_2O, Cl, and F) released during magmatic degassing. Our seismic images show that the SCLM at the cratonic edge is cut by a west-dipping XJF system (Fig. 2a, b), along which upwelling and lateral flow of the asthenosphere could trigger partial melting of the SCLM, thus endowing the carbonatitic melts.

Experiments have shown that the partial melting of mantle peridotite with CO_2 only produces SiO_2-undersaturated basaltic magmas at <80-km depths[46]. However, with increasing pressure (80–150 km) and temperature (>1200 °C), its melting could yield carbonatitic melts with silicate components[46–49]. Recent studies further suggested that incipient melts of peridotites containing both H_2O and CO_2 at 80–230 km are carbonatite[50,51], and these melts progress toward carbonated silicate compositions with increasing temperatures[50]. When the mantle contains 0.15 wt% of CO_2, carbonatites could be generated by very low degrees (<0.5%) of melting[49]. This means that the formation of the MD carbonatites requires a thick lithosphere, appropriate mantle temperatures, and a carbonated mantle source. These requirements are fully satisfied at the Yangtze cratonic margin: (1) a relatively thick underlying lithosphere (>90 km), thermally eroded by heat from asthenospheric lateral flow (Fig. 2a, b); (2) relatively high mantle temperatures (≥1000 °C) at 80- to 120-km depths (Fig. 3a), enabling partial melting of the carbonated SCLM; and (3) carbonate metasomatism in the mantle source, evidenced by light $\delta^{26}Mg$ and heavy $\delta^{66}Zn$ values of the associated Cenozoic alkaline rocks along the cratonic margin[52,53]. Note that the cratonic lithosphere was strongly thinned south of 26°N (Fig. 2c), implying the loss of a lithosphere root, where the MD carbonatites were not developed (Fig. 1a). This reinforces the concept that the carbonatitic melts resulted from the partial melting of a previously metasomatized SCLM[54,55].

REE-fertilization of the SCLM by CO_2-rich fluids from recycled marine sediments. The extreme enrichment in REEs of the MD carbonatites, through further strengthening by intra-crustal magmatic processes because of their incompatibility[2,3,21], must have undergone a refertilization process to have affected the partial-melt source. Modeling of the Sr–Nd (Fig. 3b), Hf–O (Supplementary Fig. 11), and Li–O[56] isotopic compositions of the MD carbonatites and associated syenites indicates that their SCLM sources were strongly pre-metasomatized by recycled marine sediments or fluids from a subducted slab[22,57]. The systematic increases in the ratios of La/Yb (Fig. 3c) coupled with Ce/Sr and La/Ba (Supplementary Fig. 12) for the Eocene mafic ultrapotassic magmas from the margin to the interior of the Yangtze craton probably reflect a lateral increase in the intensity of fluid metasomatism[27,58], consistent with the trajectory of continuous subduction of the oceanic lithosphere beneath the Yangtze craton since the Neoproterozoic[27].

Metasomatism by H_2O-rich fluids from subducted oceanic slabs or recycled marine sediments can hydrate, oxidize, and fertilize the SCLM with ore-forming elements (e.g., Cu and Au)[59], generating potassic–ultrapotassic magmas during later melting[45]. However, it would be difficult for this process to carbonate the mantle enough to generate carbonatite melts[60] and to explain the high Ba/Th ratios observed in the MD mafic rocks and carbonatites, because such fluids yield either a low $^{87}Sr/^{86}Sr$ close to those of midocean ridge basalts and/or have relatively low

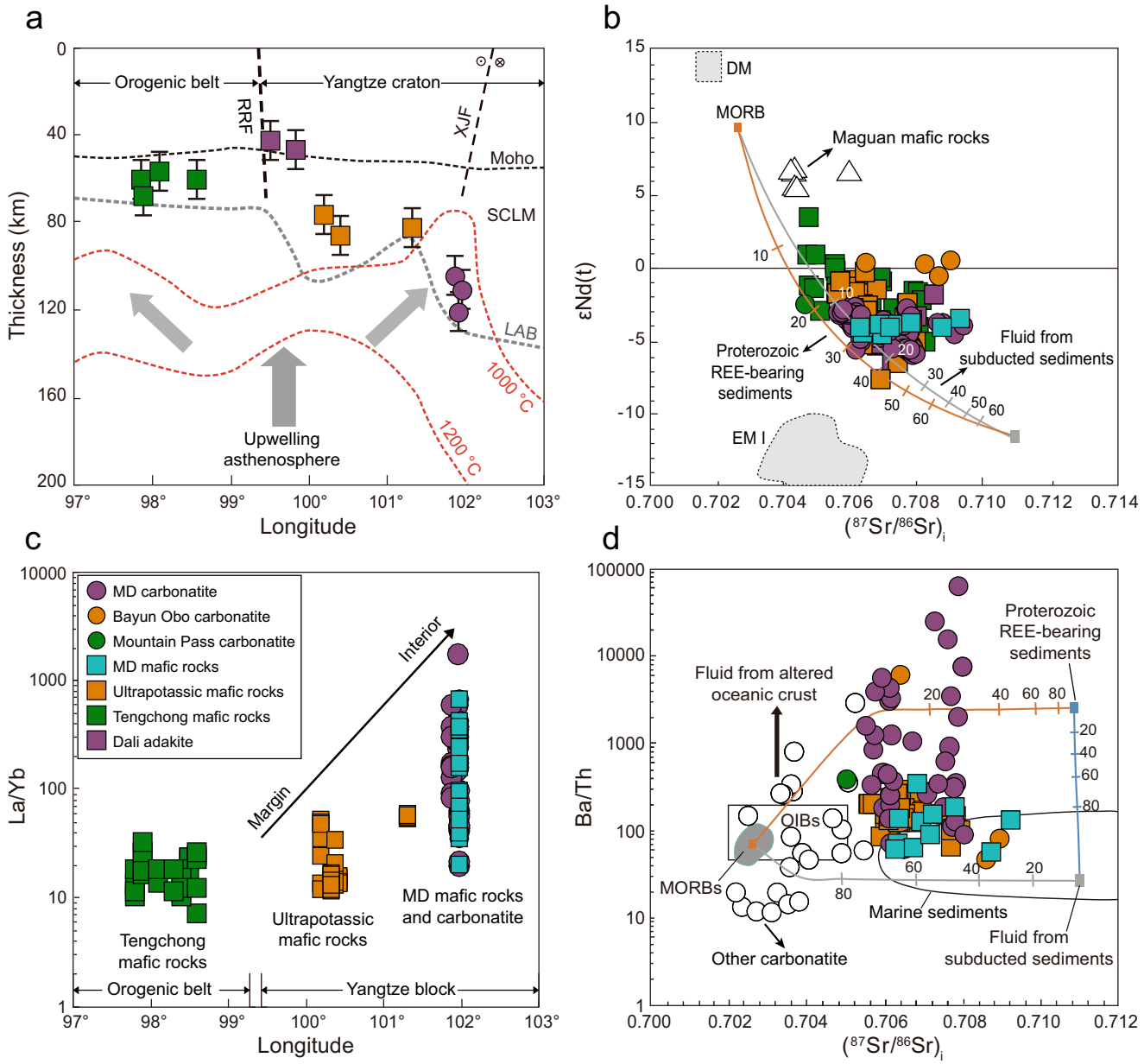

Fig. 3 Source depth and geochemical affinities of the Cenozoic magmatic rocks. a shows the relationship between the source depths for the Cenozoic magmas and the lithospheric architecture and thermal status. The bottom interface of the SCLM (i.e., LAB) is inferred from receiver function results[36] and our seismic images. The Moho is from ref. [86]. The 1000 °C and 1200 °C adiabats of the upper mantle are estimated based on our seismic data following the method of An and Shi[33]. Note that there has been no intensive magmatic activity in the western Yangtze craton after ~20 Ma (forming age of MD carbonatites), and the mantle thermal states can be preserved. The melting depth of carbonatitic melts is inferred from available experimental data (see text); others were estimated by bulk-rock La/Yb ratios using the methods of ref. [87]. Errors are two standard errors. SCLM: subcontinental lithospheric mantle; LAB: lithosphere/asthenosphere boundary; RRF: Red-River fault; XJF: Xiaojiang fault. **b** shows Sr–Nd isotopic compositions of the MD carbonatites, mafic rocks and Eocene ultrapotassic rocks at the cratonic edge, suggesting their cratonic SCLM sources metasomatized by fluids and marine sediments. Other carbonatites (e.g., Bayun Obo and Mountain Pass) were shown for comparison. The numbers on the orange (fluid from subducted sediments[88]) and gray (REE-bearing sediments[89,90]) curves represent the percentage contents of the endmembers in magma mixing models. **c** shows systematic variation in La/Yb ratio (other ratios see Supplementary Fig. 10) of the ultrapotassic rocks and the MD carbonatites and mafic rocks, reflecting a lateral increase in the intensity of fluid metasomatism toward the interior of the Yangtze craton. **d** shows the higher Ba/Th of the MD carbonatites, requiring the involvement of CO_2-rich fluids derived from recycled sediments and REE-rich sediments. Data from Supplementary Data 1–3 and ref. [21]. The numbers on the orange, blue and gray curves represent the percentage contents of the endmembers in magma mixing models. In the mixing calculation, assuming that element A mixes with element B, the binary hybrid values are given by $(Ba/Th)_{A(X\%)-B(1-X\%)} = [Th_A{*}X\%{*}(Ba/Th)_A + Th_B{*}(1-X\%){*}(Ba/Th)_B]/[Th_A{*}X\%+Th_B{*}(1-X\%)]$ and $[(^{87}Sr/^{86}Sr)_i]_{A(X\%)-B(1-X\%)} = [Sr_A{*}X\%{*}[(^{87}Sr/^{86}Sr)_i]_A + Sr_B{*}(1-X\%) * [(^{87}Sr/^{86}Sr)_i]_B]/[Sr_A{*}X\%+Sr_B{*}(1-X\%)]$.

Ba/Th (Fig. 3d). Direct melting of carbonate sediments recycled into the cratonic mantle theoretically could produce primary carbonatitic melts, but these melts would yield more radiogenic Sr isotope compositions ($^{87}Sr/^{86}Sr > 0.706$)[61] and lower Ba/Th ratios (<100) than those in the MD mafic rocks and carbonatites (Fig. 3d).

Here, we propose that CO_2-rich fluids from recycled marine sediments plus REE-rich sediments are most likely responsible for

the geochemical and isotopic characteristics of the MD mafic rocks and carbonatites inherited from the metasomatized SCLM (Fig. 3b, d). CO_2-rich fluids generally have high large-ion lithophile element (LILE) contents and LILE/high field strength element (HFSE) ratios[62]. Experiments indicate that CO_2-rich fluids could transport and add light REEs (LREEs) to the SCLM at pressures >25 kbar[47] because of the high partitioning coefficients of LREEs in CO_2-rich fluids/melts[48]. The SCLM metasomatized by such LREE- and CO_2-rich fluids would become a carbonated peridotite enriched in LILEs and REEs. The partial melting of this material would concentrate the alkaline-earth elements (e.g., Ca, Sr, and Ba) and LREEs into carbonate-rich melts[48], leaving HFSEs, heavy REEs, and residual Y in refractory rutile because of their high $D_{min/melt}$[63]. This scenario is also consistent with the thermodynamic modeling of the dehydration of subducted oceanic lithosphere, which releases 60–90% of CO_2 with increasing depth[64].

Previous studies have demonstrated that REEs are concentrated in metalliferous, Fe-oxyhydroxide-bearing sedimentary muds on the modern seafloor, such as in the southern Pacific (>1000-ppm total REE + Y) and northern Pacific (>400-ppm total REE + Y)[65]. Recent observations demonstrate that the now-exposed Mesoproterozoic (~1.6 Ga) shallow marine dolomites and phosphorites along the western margin of the Yangtze craton contain sections of exhalative-sedimentary Fe–Cu–REE mineralization[66]. These rocks provide an analog for Neoproterozoic recycled marine sediments, and they contain abundant LREE-rich bastnäsite and have total REE contents up to 4440 ppm[66]. We suggest that such REE-rich marine sediments could be the source of the metasomatizing LREE-rich and CO_2-rich fluids during Neoproterozoic subduction. These fluids strongly reacted with the overlying SCLM, generating a carbonated peridotite source for the geochemically distinctive partial-melt component of the carbonatitic magmas. This scenario is also consistent with recent Mg- and Zn-isotope studies on Cenozoic alkali basalts in the Tibetan collision orogen[52]. A simulation calculation shows that binary mixing of the depleted mantle with fluids derived from Mesoproterozoic marine sediments could also explain the high Ba/Th (>100) and $^{87}Sr/^{86}Sr$ values of the MD mafic rocks and carbonatites (Fig. 3d). We therefore suggest that preexisting REE refertilization of the SCLM produced by the Proterozoic subduction is critical for post-collisional carbonatites and associated REE deposits in the MD belt.

Formation of carbonatite-associated rare-earth element deposits. Our results reinforce three key factors previously recognized for the formation of fertile carbonatites and CARDs in collisional settings: (1) a thick lithosphere with associated high pressure (>25 kbar)[47], (2) a carbonated lithosphere mantle source enriched in REEs[22], and (3) favorable pathways for magmas ascending through the overlying crust, where additional fractionation promotes the formation of a mobile alkaline "brine-melt" and alkali REE carbonates[3,67]. We argue that the optimal configuration of all three factors at the activated craton edges is critical to the formation of giant CARDs (Fig. 4). The cratonic lithosphere in orogenic belts (e.g., collisional) is typically relatively thick, partly because it preserves a continental root (Fig. 2a, b), and the SCLM above a fossil subduction zone had previously subjected to subduction-related metasomatism with various degrees (Fig. 4). Continental subduction during collision disturbed the overlying mantle, which caused the asthenospheric upwelling along the convergent block boundaries and subsequent lateral flow beneath the rigid SCLM, as observed in Fig. 2. The head of the upwelling asthenosphere, similar to a mantle plume, can thermally erode and interact with the overlying SCLM and generate ultrapotassic magmas (Fig. 4). Asthenospheric lateral flow over time triggers partial melting of the REE-rich thick carbonated cratonic SCLM, generating carbonate-rich melts ascended along trans-lithospheric faults and/or planes of weakness (e.g., XJF) into the shallow crust near the cratonic edge (Fig. 4). Similar melting may also happen in the REE-refertilized SCLM below some rifts at the cratonic edge, along which the resulting carbonatite melts ascend upward and form CARDs in the crust (Fig. 4).

We argue that mantle metasomatism with REE refertilization prior to melting is an important prerequisite for giant CARD formation. It is likely that whether this process happened depends on the thermal states of the subduction systems and the thickness and behavior of the recycled sediments. Kinematic modeling and instability calculations indicate that the subducted oceanic crust dehydrates before it reaches subarc depths[68], while sediments detach from the downgoing slab to form buoyant diapirs at subarc depths[69]. Melting of the rising diapirs at >1000 °C would release trace elements (Th, Pb, and LREE) into arc lavas, which thus show the sediment melt signature[69] or into the overlying SCLM, which generate ultrapotassic magmas during later melting (see Fig. 4). A greater fraction of carbonate sediments may be transported to deeper mantle depths with ongoing subduction[70], where they release REE- and CO_2-rich fluids[62] or generate near-solidus small-degree partial melts[69], then metasomatized the overlying depleted SCLM (see Fig. 4). The continuous subduction processes lead to the homogeneity of the cratonic SCLM and refertilization with ore-forming elements varying from Cu–Au to REE from the margin to the interior of a craton (Fig. 4).

Our genetic model for giant REE ore systems provides a reasonable explanation for other CARDs[18,71,72]. A typical example is the Proterozoic Mountain Pass REE deposit in the United States[72], which is located at the reactivated edge (accretionary orogen) of an Archean craton[73]. The associated carbonatites originated from a metasomatized mantle source at 1.8–1.6 Ga[74]. This is also the case for the giant Bayun Obo deposit on the northern margin of the North China Craton[18]. Although the asthenospheric upwelling and lithospheric thinning strongly modified this craton since the Mesozoic[75], its ancient SCLM was metasomatized by subducted sediments at 1.9–2.0 Ga[76], and subsequent melting generated the REE-rich carbonatites and associated CARD during mid-Proterozoic rifting[2]. Some medium–small CARDs, although also located along the cratonic margins[2,17], have limited potentials and prospects. This is likely related to other factors, such as the lack of REE refertilization and strong metasomatism in the SCLM, the limited volume of carbonatic melts[2], unfavorable intracrustal magmatic processes for REE mobility and enrichment[3], and even geopolitics, environmental concerns, economics and so on. We argue that cratonic margins with REE refertilization most likely satisfy the optimally-configured conditions for generating CARDs and therefore suggest that the reactivated cratonic edges should be favorable targets for exploration of such CARDs.

Methods

To image the mantle structure of the eastern Indo-Asian collision zone, we conducted seismic tomography for continental China and its surrounding regions using teleseismic double-difference tomography method[77]. We mainly assembled two sets of data from the ISC-EHB Bulletin and China Digital Seismic Network (CDSN) catalog (Supplementary Figs. 1 and 2). The ISC-EHB Bulletin contains a refined version of the methodology described

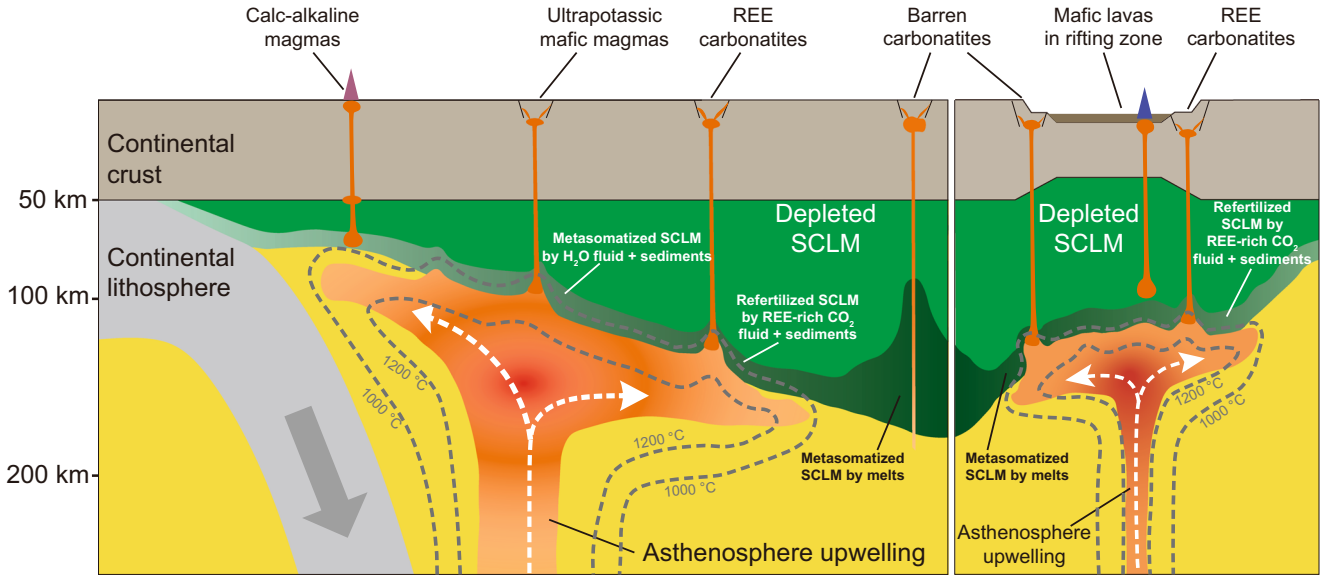

Fig. 4 A schematic cartoon illustrating the genesis of CARDs at cratonic edges. At cratonic margins, vertical upwelling and lateral flow of hot asthenosphere driven by subduction or mantle convection thermally eroded and partially melted overlying the cratonic SCLM. The SCLM at cratonic margins previously underwent metasomatism by REE- and CO_2-rich fluids from recycled marine sediments and thus refertilzed in REEs, which were entrained later by carbonate-rich melts ascending along lithospheric discontinuities (e.g., strike-slip faults; rifts), forming giant CARDs in the orogens and rifts. Melting of the cratonic SCLM with lacking source metasomatism by REE- and CO_2-rich fluids could generate carbonatic, ultrapotassic and mafic melts, but they have limited potential for CARD formation. The adiabatic temperatures of 1000 °C and 1200 °C of the upper mantle are shown (see Fig. 3a).

in ISC Bulletin by the EHB algorithm[78] to minimize errors in earthquake locations. We collected P-wave arrival times of globally distributed stations in the period of 1964–2017. For the CDSN catalog, we assembled approximately 780,000 events recorded by 1434 stations during the period from 2008/10 to 2018/06. Most events are shallow and of small magnitude. In this study, we carefully selected a limited number of events based on the following criteria. We first divided the study region into 0.5° × 0.5° × 50 km cells and only selected the first 10 events with maximum observations in each cell, and each event had more than 20 observations. As a result, 3105 events were selected from the CDSN catalog. From the two datasets, we constructed 1.69 million absolute arrival times, from which ~7.2 million event-pair differential arrival times were constructed by selecting event pairs having more than 50 common observations for the ISC-EHB Bulletin and more than 20 common observations for the CDSN. The distances between event pairs were between 50 and 500 km.

Compared with available global velocity models, our model better resolves more details in the mantle structure in the study area (Supplementary Fig. 5).

For the inversion, we followed the teleseismic double-difference seismic tomography method (teletomoDD) of ref. [78], which is a global version of the double-difference seismic tomography method (tomoDD)[79,80]. It can use both regional and teleseismic stations to invert for the velocity structure of the study region. The model is parameterized by nested grids with coarse and global grids outside the study region and finer and regional grids for the study region. For the regional initial model, we choose the AK135 model[81]. The regional model is from 74°E to 136°E in longitude and from 18°N to 54°N in latitude and extends to 2500 km in depth. The regional grid interval is 2° along longitude and latitude and ~40~300 km in depth. For the global model, we choose the TX2019slab model[82] as the initial model, with a grid interval of 5° in the horizontal direction and ~55~225 km in depth.

In the inversion, we applied a hierarchy strategy to invert for the velocity structure[79] by first giving absolute arrival times a larger weight and then giving event-pair differential times a larger weight. After seven iterations, the absolute data RMS residual decreases from 1.85 s to 0.73 s, and the weighted data residual decreases from 3.31 s to 0.56 (Supplementary Fig. 3). Compared to the data residuals with respect to the initial model, final travel time residuals are more concentrated near 0 s (Supplementary Fig. 3). We plotted different depth slices of the final Vp model for continental China and surrounding regions (Supplementary Fig. 4).

The checkerboard resolution test was used to check the model resolution. In our checkerboard test, we added ±5% anomalies at the adjacent grid nodes in the regional model. Here, we only show recovered checkerboard patterns for the eastern Indo-Asian collision zone. Supplementary Figs. 5 and 6 show the checkerboard recovery at different depths and along different latitudes. Overall, for the eastern Indo-Asian collision zone, the model has a good resolution in most parts.

Along the three profiles in Fig. 1a, we also plotted four widely used global velocity models, including the GAP_P4 model[83] (Supplementary Fig. 7a), the LLNL_G3Dv3 model[84] (Supplementary Fig. 7b), the MIT-P08 model[85] (Supplementary Fig. 7c), and the TX2019slab model[82] (Supplementary Fig. 7d). In comparison, our model (Fig. 2) shows more detailed mantle features, while the other four global models show some fuzzy and inconsistent features. This is because we used both dense regional seismic stations and teleseismic stations. For example, in the GAP_P4 model (Supplementary Fig. 7a), although the subducted Indian slab can be imaged, the Yangtze block is not well resolved. For the LLNL_G3Dv3 model (Supplementary Fig. 7b), both the Indian and Yangtze blocks are not well imaged. For the MIT-P08 model (Supplementary Fig. 7c), the amplitude of velocity anomalies is subdued and although the subducted Indian slab can be identified the Yangtze block is

very fuzzy. Lastly, the TX2019slab model also shows low-resolution features for the Indian and Yangtze blocks (Supplementary Fig. 7d). Compared to our Vp model (Fig. 2), these four models do not show clear upwelling asthenosphere from the MTZ (Supplementary Fig. 7).

Because the Vp model mostly focuses on the mantle structure of the eastern Indo-Asian collision zone, to obtain higher-resolution images for depths of 60–110 km, we also plotted Vp and Vs depth slices at 80 km of the USTClitho2.0 model inverted from joint inversion of body and surface wave data (Supplementary Fig. 8)[32]. It can also be seen that the India block and Yangtze block are in close contact at approximately 101°E, and there is a clear channel shown as low-velocity anomalies between the two blocks. This is consistent with the features observed in the depth slice of 160 km in the Vp model obtained in this study.

Data availability

Supplementary figures and geochemical datasets used in this study can be found in Supplementary Information and Supplementary Data 1–3, respectively. The tomography model for the study region is provided in Supplementary Data 4. All these materials are available online at https://doi.org/10.6084/m9.figshare.23626662.

Received: 6 August 2022; Accepted: 8 August 2023;
Published online: 19 August 2023

References

1. Xie, Y. L., Verplanck, P., Hou, Z. Q. & Zhong, R. C. Rare earth element deposits in China: a review and new understandings. *Soc. Econ. Geol. Spec. Publ.* **22**, 509–552 (2019).
2. Smith, M. P. et al. From mantle to critical zone: a review of large and giant sized deposits of the rare earth elements. *Geosci. Front.* **7**, 315–334 (2016).
3. Anenburg, M., Broom-Fendley, S. & Chen, W. Formation of rare earth deposits in carbonatites. *Elements* **17**, 327–332 (2021).
4. Weng, Z., Jowitt, S. M., Mudd, G. M. & Haque, N. A detailed assessment of global rare earth element resources: opportunities and challenges. *Econ. Geol.* **110**, 1925–1952 (2015).
5. Banks, G., Walter, B., Marks, M. & Siegfried, P. A workflow to define, map and name a carbonatite-or alkaline igneous-associated REE-HFSE mineral system: a case study from SW Germany. *Minerals* **9**, 97 (2019).
6. Banks, G. J., Olsen, S. D. & Gusak, A. A method to evaluate REE-HFSE mineralised provinces by value creation potential, and an example of application: Gardar REE-HFSE province, Greenland. *Geosci. Front.* **11**, 2141–2156 (2020).
7. Woolley, A. R. & Bailey, D. K. The crucial role of lithospheric structure in the generation and release of carbonatites: geological evidence. *Mineral. Mag.* **76**, 259–270 (2012).
8. Bell, K. & Tilton, G. R. Nd, Pb and Sr isotopic compositions of East Africa carbonatites: mantle mixing and plume inhomogeneity. *J. Petrol.* **42**, 1927–1945 (2001).
9. Woolley, A. R. & Kjarsgaard, B. A. Paragenetic types of carbonatite as indicated by the diversity and relative abundances of associated silicate rocks: evidence from a global database. *Canad. Mineralogist* **46**, 741–752 (2008).
10. Humphreys-Williams, E. R. & Zahirovic, S. Carbonatites and global tectonics. *Elements* **17**, 339–344 (2021).
11. Woolley, A. R. The spatial and temporal distribution of carbonatites. in *Carbonatites Genesis and Evolution* (ed. Bell, K.) 15–37 (Unwin Hyman, 1989).
12. Nelson, D. R., Chivas, A. R., Chappell, B. W. & Mcculloch, M. T. Geochemical and isotopic systematics in carbonatites and implications for the evolution of ocean-island sources. *Geochim. Cosmochim. Acta* **52**, 1–17 (1988).
13. Kwon, S. T., Tilton, G. R. & Grunenfelder, M. H. Pb isotope relationships in carbonatites and alkaline complexes: an overview. in *Carbonatite: Genesis and Evolution* (ed. Bell, K.) 360–387 (Unwin Hyman, 1989).
14. Bell, K. & Simonetti, A. Carbonatite magmatism and plume activity: implications from the Nd, Pb and Sr isotope systematics of OldoinyoLengai. *J. Petrol.* **37**, 1321–1339 (1996).
15. Kalt, A., Hegner, E. & Satir, M. Nd, Sr, and Pb isotopic evidence for diverse lithospheric mantle sources of East African Rift carbonatites. *Tectonophysics* **278**, 31–45 (1997).
16. Tilton, G. R., Bryce, J. G. & Mateen, A. Pb–Sr–Nd isotope data from 30 and 300 Ma collision zone carbonatites in northwest Pakistan. *J. Petrol.* **39**, 1865–1874 (1998).
17. Goodenough, K. M. et al. Carbonatites and alkaline igneous rocks in post-collisional settings: storehouses of rare earth elements. *J. Earth Sci.* **32**, 1332–1358 (2021).
18. Ling, M. X. et al. Formation of the world's largest REE deposit through protracted fluxing of carbonatite by subduction-derived fluids. *Sci. Rep.* **3**, 1–8 (2013).
19. Wang, J. H. et al. A tectonic model for Cenozoic igneous activities in the eastern Indo-Asian collision zone. *Earth Planet. Sci. Lett.* **188**, 123–133 (2001).
20. Hou, Z. Q. et al. The Himalayan Mianning-Dechang REE belt associated with carbonatite-alkalic complex in the eastern Indo-Asian collision zone, SW China. *Ore. Geol. Rev.* **36**, 65–89 (2009).
21. Hou, Z. Q. et al. The Himalayan collision zone carbonatites in western Sichuan, SW China: petrogenesis, mantle source and tectonic implication. *Earth Planet. Sci. Lett.* **244**, 234–250 (2006).
22. Hou, Z. Q., Yan, L., Tian, S. H., Yang, Z. M. Y. & Xie, L. Formation of carbonatite-related giant rare-earth-element deposits by the recycling of marine sediments. *Sci. Rep.* **5**, 10231 (2015).
23. Yaxley, G. M., Kjarsgaard, B. A. & Jaques, A. L. Evolution of carbonatite magmas in the upper mantle and crust. *Elements* **17**, 315–320 (2021).
24. Yaxley, G. M., Anenburg, M., Tappe, S., Decree, S. & Guzmics, T. Carbonatites: classification, sources, evolution, and emplacement. *Annu. Rev. Earth Planet. Sci.* **50**, 261–293 (2022).
25. Liu, Y. & Hou, Z. Q. A synthesis of mineralization styles with an integrated genetic model of carbonatite-syenite-hosted REE deposits in the Cenozoic Mianning-Dechang REE metallogenic belt, the eastern Tibetan Plateau, southwestern China. *J. Asian Earth Sci.* **137**, 35–79 (2017).
26. Yin, A. & Harrison, T. M. Geological evolution of the Himalayan-Tibetan orogen. *Annu. Rev. Earth Planet. Sci.* **28**, 211–280 (2000).
27. Guo, Z. F. et al. Potassic magmatism in Western Sichuan and Yunnan Provinces, SE Tibet, China: petrological and geochemical constraints on petrogenesis. *J. Petrol.* **46**, 33–78 (2005).
28. Liu, Y., Yao, H., Zhang, H. & Fang, H. The community velocity model V. 1.0 of southwest China, constructed from joint body- and surface-wave travel-time tomography. *Seismol. Res. Lett.* **92**, 2972–2987 (2021).
29. Feng, M. et al. Lithospheric structures of and tectonic implications for the central–east Tibetan plateau inferred from joint tomography of receiver functions and surface waves. *Geophys. J. Int.* **223**, 1688–1707 (2020).
30. Li, J. T. & Song, X. D. Tearing of Indian mantle lithosphere from high resolution seismic images and its implications for lithosphere coupling in southern Tibet. *Proc. Natl. Acad. Sci. USA* **115**, 8296–8300 (2018).
31. Wang, Z. D., Zhao, D. & Wang, J. Deep structure and seismogenesis of the north-south seismic zone in southwest China. *J. Geophys. Res.* **115**, B12334 (2010).
32. Han, S., Zhang, H., Xin, H., Shen, W. & Yao, H. USTClitho2. 0: updated unified seismic tomography models for Continental China lithosphere from joint inversion of body-wave arrival times and surface-wave dispersion data. *Seismol. Res. Lett.* **93**, 201–215 (2022).
33. An, M. & Shi, Y. Lithospheric thickness of the Chinese continent. *Phys. Earth Planet. Inter.* **159**, 257–266 (2006).
34. Zhou, X. et al. Geochemical features of hot spring gases in the Jinshajiang-Red River fault zone, Southeast Tibetan Plateau. *Acta Petrol. Sin.* **36**, 2197–2214 (2020).
35. Wu, J. P., Yang, T., Wang, W. L., Ming, Y. H. & Zhang, T. Z. Three dimensional P-wave velocity structure around Xiaojiang fault system and its tectonic implications. *Chinese J. Geophys.* **56**, 2257–2267 (2013).
36. Yang, H., Peng, H. & Hu, J. The lithospheric structure beneath southeast Tibet revealed by P and S receiver functions. *J. Asian Earth Sci.* **138**, 62–71 (2017).
37. Lev, E., Long, M. D. & van der Hilst, R. D. Seismic anisotropy in Eastern Tibet from shear wave splitting reveals changes in lithospheric deformation. *Earth Planet. Sci. Lett.* **251**, 293–304 (2006).
38. Kong, F. et al. Azimuthal anisotropy and mantle flow underneath the southeastern Tibetan Plateau and northern Indochina Peninsula revealed by shear wave splitting analyses. *Tectonophysics* **747–748**, 68–78 (2018).
39. Xu, B. et al. Cenozoic lithospheric architecture and metallogenesis in Southeastern Tibet. *Earth Sci. Rev.* **214**, 103472 (2021).
40. Hou, Z. Q. et al. Weinberg, recycling of metal-fertilized lower continental crust: origin of non-arc Au-rich porphyry deposits at cratonic edges. *Geology* **45**, 563–566 (2017).
41. Yang, Y. et al. Seismic anisotropy in the Tibetan lithosphere inferred from mantle xenoliths. *Earth Planet. Sci. Lett.* **515**, 260–270 (2019).
42. Yu, X. H., Mo, X. X., Zeng, P. S., Zhu, D. Q. & Xiao, X. N. A study on the mantle xenoliths in the Cenozoic volcanic rocks from Maguan area, Yunnan Province. *Acta Petrol. Sin.* **22**, 621–630 (2006).
43. Hou, Z. Q., Xu, B., Zheng, Y. C., Zheng, H. W. & Zhang, H. R. Mantle flow: the deep mechanism of large-scale growth in Tibetan plateau (in Chinese). *Chin. Sci. Bull.* **66**, 2671–2690 (2021).

44. Liu, F. L., Wang, F., Liu, P. H. & Liu, C. H. Multiple metamorphic events revealed by zircons from the Diancang Shan—Ailao Shan metamorphic complex, southeastern Tibetan Plateau. *Gondwana Res.* **24**, 429–450 (2013).
45. Xu, B. et al. Recycled volatiles determine fertility of porphyry deposits in collisional settings. *Am. Miner* **106**, 656–661 (2021).
46. Wyllie, P. J. & Huang, W. L. Carbonation and melting reactions in the system $CaO-MgO-SiO_2-CO_2$ at mantle pressures with geophysical and petrological applications. *Contrib. Mineral. Petrol.* **54**, 79–107 (1976).
47. Dasgupta, R. & Hirschmann, M. M. Melting in the Earth's deep upper mantle caused by carbon dioxide. *Nature* **440**, 659–662 (2006).
48. Dasgupta, R., Hirschmann, M. M., McDonough, W. F., Spiegelman, M. & Withers, A. C. Trace element partitioning between garnet lherzolite and carbonatite at 6.6 and 8.6 GPa with applications to the geochemistry of the mantle and of mantle-derivedmelts. *Chem. Geol.* **262**, 57–77 (2009).
49. Gudfinnsson, G. H. & Presnall, D. C. Continuous gradations among primary carbonatitic, kimberlitic, melilititic, basaltic, picritic, and komatiitic melts in equilibrium with garnet lherzolite at 3–8 GPa. *J. Petrol.* **46**, 1645–1659 (2005).
50. Pintér, Z. et al. Experimental investigation of the composition of incipient melts in upper mantle peridotites in the presence of CO_2 and H_2O. *Lithos* **396–397**, 106224 (2021).
51. Dasgupta, R. Volatile-bearing partial melts beneath oceans and continents–Where, how much, and of what compositions? *Am. J. Sci.* **318**, 141–165 (2018).
52. Liu, S. A., Wang, Z. Z., Yang, C., Li, S. G. & Ke, S. Mg and Zn isotope evidence for two types of mantle metasomatism and deep recycling of magnesium carbonates. *J. Geophys. Res. Solid Earth* **125**, e2020JB020684 (2020).
53. Miao, Z. et al. Deciphering mantle heterogeneity associated with ancient subduction-related metasomatism: Insights from Mg-K isotopes in potassic alkaline rocks. *Geochim. Cosmochim. Acta* **348**, 258–277 (2023).
54. Mitchell, R. H. The melilitite clan. in *Undersaturated alkaline rocks: mineralogy, petrogenesis, and economic potential* (ed. Mitchell, R. H.) 123–152 (Mineralogical Association of Canada, 1996).
55. Mitchell, R. H. Carbonatites and carbonatites and carbonatites. *Can. Mineral.* **43**, 2049–2068 (2005).
56. Tian, S. H. et al. The anomalous lithium isotopic signature of Himalayan collisional zone carbonatites in western Sichuan, SW China: enriched mantle source and petrogenesis. *Geochim. Cosmochim. Acta* **159**, 42–60 (2015).
57. Xu, B. et al. Apatite halogens and Sr–O and zircon Hf–O isotopes: recycled volatiles in Jurassic porphyry ore systems in southern Tibet. *Chem. Geol.* **605**, 120924 (2022).
58. Shen, Y. et al. Petrology of the Machangqing complex in Southeastern Tibet: implications for the genesis of potassium-rich adakite-like intrusions in collisional zones. *J. Petrol.* **62**, egab066 (2021).
59. Griffin, W. L., Begg, G. C. & O'reilly, S. Y. Continental-root control on the genesis of magmatic ore deposits. *Nat. Geosci.* **6**, 905–910 (2013).
60. Bell, K. & Simonetti, A. Source of parental melts to carbonatites–critical isotopic constraints. *Mineral. Petrol.* **98**, 77–89 (2010).
61. Ohtman, D. B., White, W. M. & Patchett, J. The geochemistry of marine sediments, island arc magma genesis, and crust-mantle recycling. *Earth Planet. Sci. Lett.* **94**, 1–21 (1989).
62. Elburg, M. A. et al. Geochemical trends across an arc–continent collision zone: magma sources and slab–wedge transfer processes below the Pantar Strait volcanoes, Indonesia. *Geochim. Cosmochim. Acta* **66**, 2771–2789 (2002).
63. Gaetani, G. A., Asimow, P. D. & Stolper, E. M. A model for rutile saturation in silicate melts with applications to eclogite partial melting in subduction zones and mantle plumes. *Earth Planet. Sci. Lett.* **272**, 720–729 (2008).
64. Ague, J. & Nicolescu, S. Carbon dioxide released from subduction zones by fluid-mediated reactions. *Nat. Geosci.* **7**, 355–360 (2014).
65. Kato, Y. et al. Deep-sea mud in the Pacific Ocean as a potential resource for rare-earth elements. *Nat. Geosci.* **4**, 535–538 (2011).
66. Yang, Y. M., Tu, G. Z. & Hu, R. Z. REE and trace element geochemistry of Yinachang Fe-Cu-REE deposit, Yunnan province, China. *Chin. J. Geochem.* **23**, 256–274 (2004).
67. Anenburg, M., Mavrogenes, J. A., Frigo, C. & Wall, F. Rare earth element mobility in and around carbonatites controlled by sodium, potassium, and silica. *Sci. Adv.* **6**, eabb6570 (2020).
68. Syracuse, E. M., van Keken, P. E. & Abers, G. A. The global range of subduction zone thermal models. *Phys. Earth Planet. Inter.* **183**, 73–90 (2010).
69. Behn, M. D., Kelemen, P. B., Hirth, G., Hacker, B. R. & Massonne, H. Diapirs as the source of the sediment signature in arc lavas. *Nat. Geosci.* **4**, 641–646 (2011).
70. Molina, J. F. & Poli, S. Carbonate stability and fluid composition in subducted oceanic crust: an experimental study on $H_2O–CO_2$-bearing basalts. *Earth Planet. Sci. Lett.* **176**, 295–310 (2000).
71. Anenburg, M., Mavrogenes, J. A. & Bennett, V. C. The fluorapatite P–REE–Th vein deposit at nolans bore: genesis by carbonatite metasomatism. *J. Petrol.* **61**, egaa003 (2020).
72. Castor, S. B. The Mountian Pass rare-earth carbonatite and associated ultrapotassic rocks, California. *Can. Mineral.* **46**, 779–806 (2008).
73. Whitmeyer, S. J. & Karl, E. K. Tectonic model for the Proterozoic growth of North America. *Geosphere* **3**, 220–259 (2007).
74. Watts, K. E., Haxel, G. B. & Miller, D. M. Temporal and petrogenetic links between mesoproterozoic alkaline and carbonatite magmas at Mountain Pass, California. *Econ. Geol.* **117**, 1–23 (2021).
75. Zhu, R. X., Yang, J. H. & Wu, F. Y. Timing of destruction of the North China Craton. *Lithos* **149**, 51–60 (2012).
76. Zhai, M. G. et al. Two linear granite belts in the central-western North China Craton and their implication for late Neoarchean-Paleoproterozoic continental evolution. *Precambrian Res.* **127**, 267–283 (2003).
77. Engdahl, E. R., van der Hilst, R. & Buland, R. Global teleseismic earthquake relocation with improved travel times and procedures for depth determination. *Bull. Seismol. Soc. Amer* **88**, 722–743 (1998).
78. Pesicek, J. D., Zhang, H. & Thurber, C. H. Multiscale seismic tomography and earthquake relocation incorporating differential time data: application to the Maule subduction zone, Chile. *Bull. Seismol. Soc. Amer.* **104**, 1037–1044 (2014).
79. Zhang, H. & Thurber, C. H. Double-difference tomography: the method and its application to the Hayward Fault, California. *Bull. Seismol. Soc. Amer.* **93**, 1875–1889 (2003).
80. Zhang, H. & Thurber, C. Development and applications of double-difference seismic tomography. *Pure. Appl. Geophys.* **163**, 373–403 (2006).
81. Kennett, B. L. N., Engdahl, E. R. & Buland, R. Constraints on seismic velocities in the Earth from traveltimes. *Geophys. J. Int.* **122**, 108–124 (1995).
82. Lu, C., Grand, S. P., Lai, H. & Garnero, E. J. TX2019slab: a new P and S tomography model incorporating subducting slabs. *J. Geophys. Res. Solid Earth* **124**, 11549–11567 (2019).
83. Obayashi, M. et al. Finite frequency whole mantle P wave tomography: improvement of subducted slab images. *Geophys. Res. Lett.* **40**, 5652–5657 (2013).
84. Simmons, N. A., Myers, S. C., Johannesson, G. & Matzel, E. LLNL-G3Dv3: Global P wave tomography model for improved regional and teleseismic travel time prediction. *J. Geophys. Res. Solid Earth* **117**, B10302 (2012).
85. Li, C., van der Hilst, R. D., Engdahl, E. R. & Burdick, S. A new global model for P wave speed variations in Earth's mantle. *Geochem. Geophys. Geosyst.* **9**, 1–21 (2008).
86. He, R., Shang, X., Yu, C., Zhang, H. & Van der Hilst, R. D. A unified map of Moho depth and Vp/Vs ratio of continental China by receiver function analysis. *Geophys. J. Int.* **199**, 1910–1918 (2014).
87. Profeta, L. et al. Quantifying crustal thickness over time in magmatic arcs. *Sci. Rep.* **5**, 1–7 (2015).
88. Plank, T. & Langmuir, C. H. The chemical composition of subducting sediment and its consequences for the crust and mantle. *Chem. Geol.* **145**, 325–394 (1998).
89. Bertram, C. J., Elderfield, H., Aldridge, R. J. & Conway Morris, S. $^{87}Sr/^{86}Sr$,$^{143}Nd/^{144}Nd$ and REEs in Silurian phosphatic fossils. *Earth Planet. Sci. Lett.* **113**, 239–249 (1992).
90. Shields, G. & Stille, P. Diagenetic constraints on the use of cerium anomalies as palaeoseawater redox proxies: an isotopic and REE study of Cambrian phosphorites. *Chem. Geol.* **175**, 29–48 (2001).

Acknowledgements

This research was funded by National Key R&D Program of China (2022YFF0800902); National Natural Science Foundation of China (42222304, 42073038); National Key Technologies R&D Program 2019YFA0708602, 2020YFA0714800; National Natural Science Foundation of China (42230101, 42073038, 41803045), Young Talent Support Project of CAST, the Fundamental Research Funds for the Central Universities (Grant no. 265QZ2021012). This is contribution 1774 from the ARC Centre of Excellence for Core to Crust Fluid Systems (http://www.ccfs.mq.edu.au) and 1542 in the GEMOC Key Centre (http://www.gemoc.mq.edu.au) and is related to IGCP-662 and DDE Big Science Program. This is the 18th contribution of Bo Xu for National Mineral Rock and Fossil Specimens Resource Center.

Author contributions

Z.Q.H. designed and initiated the research, interpreted the data and wrote the manuscript. B.X. interpreted the data and revised the manuscript. H.Z. conducted seismic tomography analysis and wrote some of the manuscript. Y.C.Z., R.W., Y.L., Z.Z., W.L.G., and S.Y.O. contributed to the design of the study and discussion of the result. Z.M. and L.G. provided figures and collected data. All the authors contributed to the interpretation of the results and the polishing of the manuscript.

Competing interests

The authors declare no competing interests.

Additional information

Supplementary information The online version contains supplementary material available at https://doi.org/10.1038/s43247-023-00956-6.

Correspondence and requests for materials should be addressed to Zeng-Qian Hou, Bo Xu or Haijiang Zhang.

Peer review information *Communications Earth & Environment* thanks Wei-Dong Sun, Kathryn Moore, Michael Anenburg, Xiaodong Song and the other, anonymous, reviewer(s) for their contribution to the peer review of this work. Primary Handling Editors: Maria Luce Frezzotti and Joe Aslin.

Reprints and permission information is available at http://www.nature.com/reprints

Publisher's note Springer Nature remains neutral with regard to jurisdictional claims in published maps and institutional affiliations.

Open Access This article is licensed under a Creative Commons Attribution 4.0 International License, which permits use, sharing, adaptation, distribution and reproduction in any medium or format, as long as you give appropriate credit to the original author(s) and the source, provide a link to the Creative Commons licence, and indicate if changes were made. The images or other third party material in this article are included in the article's Creative Commons licence, unless indicated otherwise in a credit line to the material. If material is not included in the article's Creative Commons licence and your intended use is not permitted by statutory regulation or exceeds the permitted use, you will need to obtain permission directly from the copyright holder. To view a copy of this licence, visit http://creativecommons.org/licenses/by/4.0/.

© The Author(s) 2023